

1 Mapping sequences can bias population receptive field estimates

2

3 Elisa Infanti¹, D. Samuel Schwarzkopf^{1,2}

4 ¹ UCL Experimental Psychology, 26 Bedford Way, London WC1H 0AP, UK

5 ² School of Optometry & Vision Science, University of Auckland, 85 Park Road, New Zealand

6

7

8 Key words: pRF, population receptive field, mapping, visual cortex, vision

9

10

11 Abstract

12 Population receptive field (pRF) modelling is a common technique for estimating the stimulus-
13 selectivity of populations of neurons using neuroimaging. Here, we aimed to address if pRF
14 properties estimated with this method depend on the spatio-temporal structure and the
15 predictability of the mapping stimulus. We mapped the polar angle preference and tuning width of
16 voxels in visual cortex (V1-V4) of healthy, adult volunteers. We compared sequences orderly
17 sweeping through the visual field or jumping from location to location employing stimuli of
18 different width (45° vs 6°) and cycles of variable duration (8s vs 60s). While we did not observe
19 any systematic influence of stimulus predictability, the temporal structure of the sequences
20 significantly affected tuning width estimates. Ordered designs with large wedges and short cycles
21 produced systematically smaller estimates than random sequences. Interestingly, when we used
22 small wedges and long cycles, we obtained larger tuning width estimates for ordered than random
23 sequences. We suggest that, ordered and random mapping protocols show different susceptibility
24 to other design choices such as stimulus type and duration of the mapping cycle and can produce
25 significantly different pRF results.

26

27

28

29 Introduction

30

31 Topographic organization is a fundamental principle of the human sensory brain and the study of
32 its properties plays a crucial role in understanding how the brain responds adaptively to properties
33 of the environment and current goals. Important progress in brain mapping was encouraged by the
34 introduction of population receptive field (pRF) modelling by Dumoulin & Wandell (2008). This
35 approach aims at estimating the aggregate receptive field of all neurons within a voxel in functional
36 magnetic resonance imaging (fMRI) scans. Essentially, a pRF identifies the location in sensory
37 space that drives a voxel's response, the spread of the responsive region and its shape (Dumoulin
38 & Wandell, 2008; Silson, Reynolds, Kravitz, & Baker, 2018; Wandell & Winawer, 2015;
39 Zeidman, Silson, Schwarzkopf, Baker, & Penny, 2018; Zuiderbaan, Harvey, & Dumoulin, 2012).
40 A flourishing literature in the past ten years has shown that pRF modelling constitutes a powerful
41 and sensitive approach for describing the fundamental properties of human visual cortex. The pRF
42 size increases with increasing eccentricity and along the visual hierarchy (Amano, Wandell, &
43 Dumoulin, 2009; Dumoulin & Wandell, 2008). Heterogeneities in pRF properties have been
44 revealed also between different portions of the visual field (Moutsiana et al., 2016; Silson et al.,
45 2018; Silva et al., 2018), across individuals (Moutsiana et al., 2016) and across populations
46 (Anderson et al., 2016; Schwarzkopf, Anderson, de Haas, White, & Rees, 2014; Smittenaar,
47 Macsweeney, Sereno, & Schwarzkopf, 2016). Moreover, pRF properties have been used to
48 investigate neural plasticity of the visual system during development (Dekker, Schwarzkopf, de
49 Haas, Nardini, & Sereno, 2017, 2019; Gomez, Natu, Jeska, Barnett, & Grill-Spector, 2018) or
50 evaluate adaptive changes in the human brain resulting from diseases or trauma with pRF changes
51 mirroring changes in visual function (Dumoulin & Knapen, 2018).

52 Interestingly, recent studies have also shown that pRF properties flexibly adapt to how observers
53 engage with the stimulus. Changes in the locus of attention induce shifts in pRFs preferred location
54 in the direction of the attended location across the entire visual field (Kay, Weiner, & Grill-Spector,
55 2015; Klein, Harvey, & Dumoulin, 2014; Sheremata & Silver, 2015; Vo, Sprague, & Serences,
56 2017). Such global changes are larger in higher visual areas (Klein et al., 2014) along both the
57 ventral (Kay et al., 2015) and the dorsal stream (Sheremata & Silver, 2015). Moreover, recent
58 studies indicate that pRF size and eccentricity vary in concert when the task requires to move the
59 focus of attention from fixation to the mapping stimulus, suggesting that processing resources are

60 adaptively redistributed to optimize the sampling of the visual stimulus according to task
61 requirements (Kay et al., 2015; van Es, Theeuwes, & Knapen, 2018). Similarly, changes in spatial
62 tuning of population receptive field and in their eccentricity have been observed as a consequence
63 of changes in attentional load at fixation (de Haas, Schwarzkopf, Anderson, & Rees, 2014).
64 One aspect this literature has mostly overlooked is the influence of spatial predictability of visual
65 stimuli in mapping estimates. Phase-encoded retinotopic mapping experiments (Engel et al., 1994;
66 Sereno et al., 1995) and most pRF studies (e.g. Dumoulin & Wandell, 2008; Harvey & Dumoulin,
67 2011; Moutsiana et al., 2016; van Dijk, de Haas, Moutsiana, & Schwarzkopf, 2016; Yildirim,
68 Carvalho, & Cornelissen, 2018 with few exceptions, e.g. Binda, Thomas, Boynton, & Fine, 2013;
69 Kay et al., 2015; Thomas et al., 2015) typically employ ordered stimulus sequences - such as
70 rotating wedges, contracting and expanding rings, or sweeping bars - to map visual areas. In such
71 designs, the orderly presentation of the stimulus carries an inherent spatiotemporal regularity in
72 the mapping sequence. Such regularity has two main consequences: 1) the predictability of the
73 stimulus location, 2) the systematic consecutive stimulation of adjacent spatial locations.
74 Both consequences could result in fMRI responses beyond the directly stimulated voxels.
75 Specifically, the position of a coherently moving stimulus can be anticipated based on its current
76 location and the direction of motion. The predictability of the stimulus location could induce an
77 anticipatory response in such locations (Ekman, Kok, & de Lange, 2017). Moreover, knowledge
78 of the upcoming stimulus location can provide spatial cues to direct attention to the relevant portion
79 of the screen affecting pRF estimates accordingly (Kastner, Pinsk, De Weerd, Desimone, &
80 Ungerleider, 1999). On the other hand, the consecutive stimulation of adjacent locations in space
81 can generate a “traveling wave” of activity across the cortical surface that would cause the BOLD
82 signal to spread across neighboring voxels (Engel et al., 1994). The permeability of pRF estimates
83 to spatiotemporal properties of the sequences has important implications also for the reliability of
84 the estimated parameters.

85 In a study aiming to minimize biases when measuring visual cortex reorganization, Binda and
86 colleagues (2013) compared pRF estimates using ordered sequences (i.e. sweeping bars) and m-
87 sequences of multifocal stimuli. The multifocal method consists in the presentation of multiple
88 visual stimuli presented at different locations designed to minimize the spatiotemporal correlation
89 of visual stimulation (Vanni et al., 2005). They fitted a standard 2D-Gaussian model to voxel
90 responses and observed that pRF size estimates (σ) in areas V1-V3 were systematically larger

91 when ordered mapping sequence were employed. The authors suggested that differences in the
92 mapping sequence can lead to different pRF estimates, but they did not directly address the
93 distinctive impact of expectations and spatiotemporal regularities. Moreover, in this study the two
94 mapping protocols differed not only in their spatiotemporal sequence dependencies, but also in
95 stimulus shape and size, field coverage, and scanning protocol.

96 In this study, we aim to characterize to what extent spatiotemporal regularities in the mapping
97 sequence affect the pRF parameter estimates in visual cortex, disentangling the role of spatial
98 expectations and the impact of non-linear summation of the BOLD signal when adjacent locations
99 are stimulated over a short interval. We employed functional MRI and a pRF mapping approach
100 (Dumoulin & Wandell, 2008) to estimate the polar angle preference and the tuning response of
101 voxels in visual cortex. We tested the same participants in three fMRI experiments using mapping
102 sequences that differed in the spatial contingencies of consecutive wedge stimuli and in their
103 predictability: ordered (rotating clockwise or anticlockwise), predictable, and unpredictable. In
104 addition, we compared sequences employing stimuli of different width (wedge angle of 45deg vs
105 6deg) that covered the entire visual field in cycles of variable duration (9s vs 60s). We modelled
106 pRFs of polar angle as a circular Gaussian tuning function with two parameters: the polar angle
107 preferred response and its spread quantified as full-width half-maximum (FWHM). We compared
108 polar angle estimates and tuning functions of pRFs in functionally defined occipital ROIs (V1, V2,
109 V3, V3A, V4) based on the individual maps obtained from an independent mapping experiment
110 using typical methods. Finally, we compared empirical results and simulated data as an aid for
111 understanding the biases and reliabilities of pRF estimates.

112 Results suggest that the spatiotemporal regularities in the mapping protocol significantly affected
113 pRF size (tuning width) estimates in agreement with what was previously observed for pRF size
114 in the visual (Binda et al., 2013) and the auditory domain (Thomas et al., 2015). Moreover, we
115 observed that the direction of the effect depended on the duration of the mapping cycle. Our results,
116 however, do not indicate any reliable influence of stimulus predictability on pRF properties.
117 Finally, we observed that while the ordered sequence led to the highest goodness of fit, the
118 parameters estimated in this condition were not superior to those obtained with random conditions.

119 Experiment 1

120 Here we asked whether the spatiotemporal structure of mapping sequences used in retinotopic
121 mapping experiments influences the resulting parameter estimates. In particular, we tested whether
122 pRF parameters depend on the subsequent stimulation of adjacent locations that characterize
123 ordered mapping protocols by contrasting an *ordered rotating condition* with a random one. We
124 further tested the hypothesis that such effects on parameter estimates depend on the predictability
125 of the stimulus location by contrasting a predictable, non-ordered, condition with a random one.

126 Materials and methods

127 Participants

128 Five experienced participants took part in two sessions of the experiment (1 author; age range:
129 [24-35]; 4 females; one left-handed). All participants had normal or corrected-to-normal visual
130 acuity. Participants gave their written informed consent to take part in the study and were
131 financially compensated for their participation. All procedures were approved by the University
132 College London Research Ethics Committee.

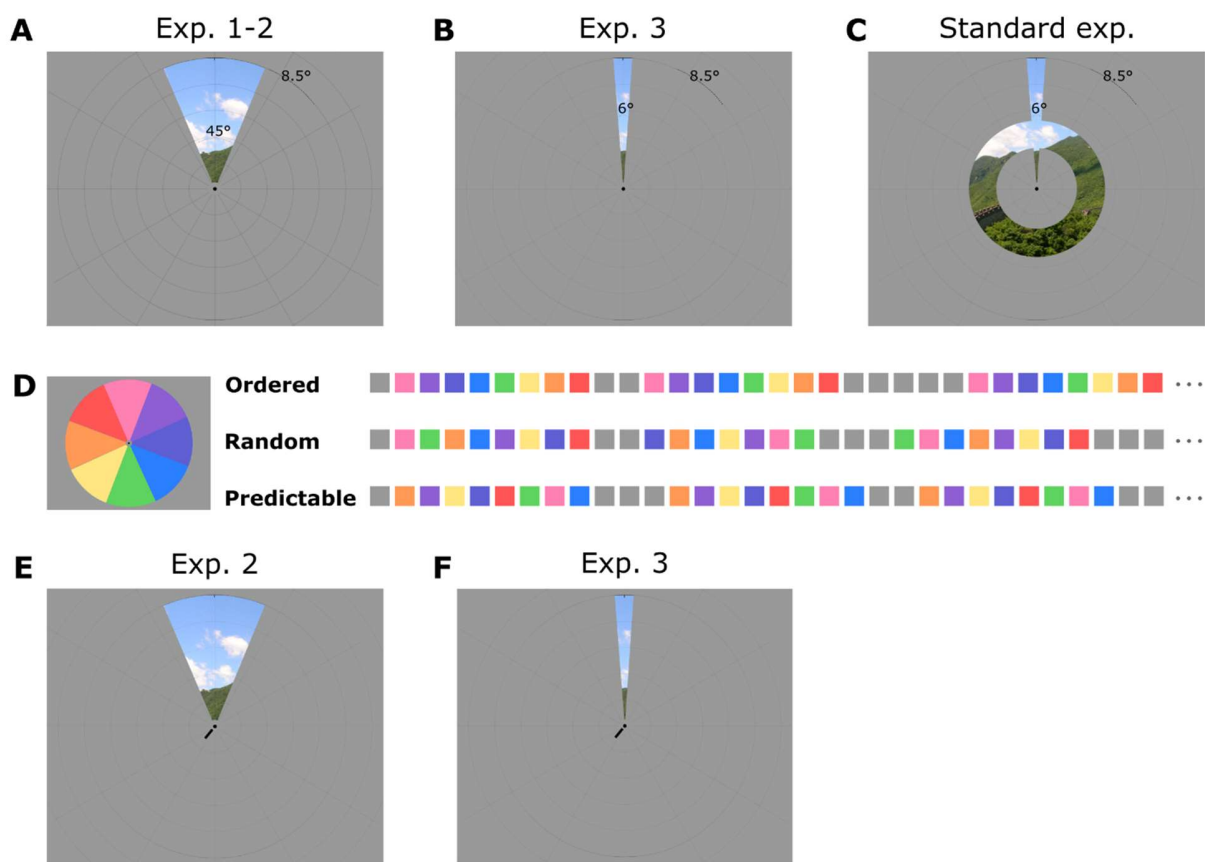
133 Stimuli and Task

134 Stimuli were presented using a custom MATLAB script (Mathworks Inc., Massachusetts, USA)
135 and the Psychophysics Toolbox 3.8 (Brainard, 1997; Pelli, 1997). They were projected on a screen
136 (1920 x 1080 pixels; 36.8 x 20.2 cm) at the back of the scanner bore and presented by means of a
137 mirror mounted on the head coil at a total viewing distance of approximately 68 cm.

138 The mapping stimulus was a discretely moving wedge-shaped aperture that showed coloured
139 natural images (1080 x 1080 pixels) depicting landscapes, textures, animals, faces, or pieces of
140 writing randomly redrawn every 500 ms and presented on a mid-grey background. The wedge
141 aperture extended from 0.38 to 8.5 degrees of visual angle (dva) in eccentricity. Each wedge
142 aperture subtended 45° in terms of polar angle and was centred at one of eight polar angles (0°,
143 45°, 90°, 135°, 180°, 225°, 270°, 315°) dividing the circle in 8 non-overlapping locations (Figure
144 1A). The centre of the wedges was shifted by 15° in separate runs in order to increase the spatial
145 granularity of the mapping.

146 Participants were instructed to continually maintain their gaze on a central fixation dot with a
147 diameter of 0.13° while covertly monitoring the movement of the mapping stimuli in the surround.
148 To ensure that both requirements were met, we used a dual-detection task in which participants

149 had to report whether the colour of the fixation dot turned red (fixation task) and whether an
150 Anderson tartan pattern was presented on the wedges (image detection task) (Moutsiana et al.,
151 2016; van Dijk et al., 2016). To aid participant's compliance with fixation requirements, a low
152 contrast polar grid (line width of 0.02° ; opacity of 10.2%) composed of 10 circles (radii evenly
153 spaced between 0.13° and 15.14°) and 12 evenly spaced radial lines extended from fixation to the
154 edges of the screen was superimposed onto the grey foreground and stimuli at all time. Eye
155 movements were further monitored by means of an MRI-compatible SR Research EyeLink 1000
156 eye tracker.



157
158 *Figure 1. Stimuli and mapping sequences for Experiments 1-3 and the standard 2D mapping experiment. A) Large wedge*
159 *mapping stimuli used in Experiments 1-2, B) thin wedge mapping stimulus used in Experiment 3, and C) wedge-and-ring*
160 *mapping stimulus used in the Standard experiment. D) Spatiotemporal structure for ordered, random and predictable sequences*
161 *in Experiment 1, each square represents 1 s and the colour denotes the polar angle (see colour wheel). E-F) Central cue used in*
162 *predictable and random-cue sequences in Experiment 2 and 3.*

163 Mapping sequences

164 Three mapping conditions were presented to each participant: *ordered*, *predictable* and *random*
165 (i.e. unpredictable) (Figure 1D). In the ordered runs, the wedge rotated around fixation either
166 clockwise or anticlockwise starting randomly at one of the 8 locations. The same direction of
167 motion and the same starting location was maintained within each run. In the predictable runs, the
168 wedge was presented at the 8 locations according to a predefined pseudorandomized order such
169 that no adjacent locations were stimulated one after the other. The sequence started at a random
170 location in different runs, but the same starting point and the same order were maintained
171 throughout the run. Six maximally distinctive sequences were selected for each participant, three
172 for each session. In the unpredictable runs, wedges were presented at the 8 locations in
173 pseudorandom order (no adjacent locations could be presented in a row) and from a random
174 starting point. A different, randomly generated, sequence was presented in each cycle (Figure 1D).
175 For all conditions, each step of the wedge was presented for 1 s such that an entire cycle was
176 completed in 8 s. The wedge completed 16 cycles in each run. Cycles were separated by fixation
177 intervals of variable duration pseudo-randomized to range from 1 to 8 s in discrete steps of 1 s.
178 Before entering in the scanner, participants performed a 30-minute task to familiarize themselves
179 with the predictable sequences that they would encounter during the scanning session. Each
180 sequence was presented in a separate block. Each block started with a presentation of the 8-steps
181 sequence, presented for 7 times, after which we introduced a violation of the location order in the
182 sequence. The participant's task was to detect this violation of regularity and report it with a button
183 press. Each sequence was presented in 6 consecutive blocks and was presented 20 times per block
184 (9 correct sequences and 11 sequences with violations). In the scanner, a familiarization block
185 preceded each mapping run in order to familiarize participants with the sequence that they would
186 encounter during the following scanning run. Similar familiarization blocks were repeated before
187 each run of the ordered and random conditions. For both the ordered and the predictable condition,
188 participants performed a sequence violation-detection task in which they reported when a wedge
189 appeared in an unexpected location according to the learned sequence (predictable condition) or
190 the direction of motion (ordered condition). In the random condition, participants performed a 2-
191 back task in which they reported when a stimulus was presented in a location that was occupied 2
192 stimuli before.

193 Reference retinotopic maps were obtained for each participant in an additional experiment using a
194 combined wedge-and-ring aperture (Figure 1C) similar to what has been reported in previous
195 studies (Alvarez, de Haas, Clark, Rees, & Schwarzkopf, 2015; Moutsiana et al., 2016; van Dijk et
196 al., 2016). The wedge aperture extended up to 8.5 degrees of visual angle in eccentricity and
197 subtended 12° rotating either clockwise or counter-clockwise in 60 discrete steps (1 step/s, 6°
198 overlap between consecutive wedges). The ring aperture expanded or contracted in 36 logarithmic
199 steps while keeping the radius of the inner circle 56-58% of that of the outer ring (minimal radius
200 of 0.48 dva, 1 step/s, ~90% overlap between consecutive rings). The mapping stimulus showed
201 coloured natural images or phase-scrambled versions of them that changed every 500 ms and
202 appeared on a mid-grey background. The type of image (intact vs phase-scrambled) alternated
203 every 15 s. The images and the wedge-and-ring aperture were centred on a central black fixation
204 dot (diameter: 0.13 degrees in visual angle) which was superimposed onto central disk (diameter:
205 0.38 degrees in visual angle). Also, a low contrast polar grid was superimposed on the stimulus.
206 As for the previous experiments, participants performed a dual-detection task (fixation task and
207 image detection task) while maintaining fixation on the central fixation dot.

208 The mapping experiment consisted of 3 runs. The wedge-and-ring aperture was presented in four
209 blocks of 90 s (1.5 cycles of wedge rotation; 2.5 cycles of ring expansion/contraction) interleaved
210 with a 30 s blank interval. The order of aperture movement in each run was first clockwise and
211 expanding, then clockwise and contracting, anticlockwise and expanding, or anticlockwise and
212 contracting.

213 Data acquisition

214 We acquired functional and anatomical scans using a Siemens Avanto 1.5 T MRI scanner with a
215 customized 32-channel head coil located at the Birkbeck-UCL Centre for Neuroimaging. The two
216 anterior channels were removed from the front half of the coil to allow unrestricted field of view
217 leaving 30 effective channels.

218 Functional images were acquired using a T2*- weighted 2D echo-planar images multi-band
219 (Breuer et al., 2005) sequence (TR = 1 ms, TE = 55 ms, 36 slices, flip angle = 75°, acceleration =
220 4, FOV = 96 × 96 voxels) at a resolution of 2.3 mm isotropic voxels. Each functional scan consisted
221 of 222 acquisitions. Data were collected in two sessions (performed on consecutive days or one

222 day apart) of 9 runs each taking approximately 90 minutes¹. Each condition was repeated in 3
223 separate runs in each session. The order of runs was pseudo-randomized, with all conditions
224 repeated every 3 runs. The ring-and-wedge mapping procedure was acquired in a separate session
225 using the same protocol, for a total of 3 runs and 490 volumes per run.

226 A T1-weighted anatomical magnetization-prepared rapid acquisition with gradient echo
227 (MPRAGE) image was acquired in a separate session (TR = 2730 ms, TE = 3.57 ms, 176 sagittal
228 slices, FOV = 256 × 256 voxels) at a resolution of 1 mm isotropic voxels.

229 *fMRI pre-processing*

230 The data were pre-processed using SPM12 (www.fil.ion.ucl.ac.uk/spm, Wellcome Centre for
231 Human Neuroimaging, London, UK). The first 10 volumes of each run were discarded to allow
232 the signal to reach equilibrium. Functional images were intensity bias-corrected, realigned to the
233 mean image of each run and then co-registered to the structural scan. All further analyses were
234 performed using custom MATLAB code. The time series for each voxel in each run were linearly
235 de-trended and z-score normalized. Finally, all runs belonging to the same condition were
236 concatenated before further analyses whereas in the wedge-and-ring standard mapping experiment,
237 the time series were averaged before the fitting analysis to increase signal to noise ratio. Functional
238 data of each participant were projected on a surface reconstruction of the grey white matter surface
239 estimated with FreeSurfer (Dale, Fischl, & Sereno, 1999; Fischl, Sereno, & Dale, 1999) by finding
240 the voxel at the medial position between the grey-white matter boundary and the pial surface for
241 each vertex in the mesh (using custom made Matlab scripts and SamSrf toolbox). All the following
242 analyses were performed at the surface level. The same procedures were adopted for Experiment
243 2 and 3.

244 *pRF estimates*

245 The data from the different protocols were used to obtain independent estimates of the population
246 receptive fields (pRFs) using a custom MATLAB toolbox for pRF analysis (SamSrf v5.84,
247 <https://doi.org/10.6084/m9.figshare.1344765.v24>). For all mapping sequences, we combined a
248 binary aperture describing the position of the mapping stimuli within each scanning volume with
249 a model of the underlying neuronal population and convolved this with a canonical haemodynamic
250 response function (HRF) to predict the BOLD signal in each experimental condition. For the

¹ One participant performed 15 runs in one single session in Experiment 1.

251 standard wedge and ring mapping sequence, the binary aperture was a two-dimensional mask
252 (100x100) corresponding to the stimulus location on the screen at each time point. For the main
253 experiment, the binary aperture was a vector mask (1x360) indicating the polar angle coordinates
254 corresponding to the mapping stimulus at each time point.

255 For the standard wedge and ring mapping sequence, we estimated the position and size of pRFs
256 using a two-dimensional Gaussian function (Dumoulin & Wandell, 2008). For the polar mapping
257 experiments, we modelled pRFs using a von Mises distribution, with μ indicating the preferred
258 polar angle of the voxel and k corresponding to the concentration of the response (for clarity k
259 values were transformed into full width half maximum (FWHM) as an indicator of the spread of
260 the response of each voxel). We used a coarse-to-fine approach to determine the pRF parameters
261 to obtain the best possible fit of the predicted time series with the observed data (Alvarez et al.,
262 2015; Dumoulin & Wandell, 2008; Moutsiana et al., 2016; van Dijk et al., 2016). The final fine
263 fitting also included a β parameter for the response amplitude.

264 Analyses

265 We only analysed the fitted parameters of those vertices for which we obtained realistic estimates
266 ($k > 0$) and that had a goodness of fit, R^2 , higher than a critical value based on a fixed p-value ($p =$
267 10^{-8}). This corresponds to $R^2 > 0.026^2$ in Experiment 1, and $R^2 > 0.067$ in the wedge-and-ring
268 experiment depending on the different degrees of freedom in the three experiments³.

269 The pRF estimated coordinates from the standard wedge and ring mapping experiment were used
270 to compute polar angle and eccentricity. Using the Delineation toolbox in SamSrf, we manually
271 delineated the regions of interest using mirror reversals in the polar angle map, and guided by the
272 eccentricity and field-sign map (Sereno, McDonald, & Allman, 1994). The region of interests
273 included in our analyses were V1, V2, V3, V3A and V4. We performed all the following analyses
274 separately for each visual ROI in each individual participant. Given the small number of
275 participants, we did not report group statistics in the main text, but we summarized the results for
276 single subject statistics instead.

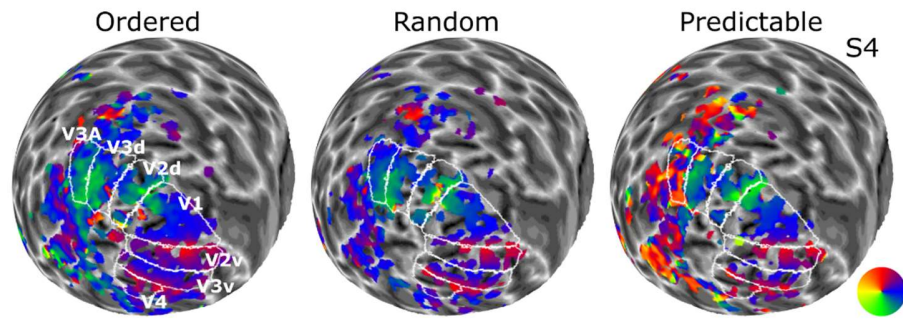
² The R^2 threshold was adjusted to 0.035 for the participant that performed a smaller number of runs in Experiment 1.

³ Here we are not accounting for the degrees of freedom in the pRF model (the p-value would only be marginally different) but the purpose of this procedure is simply to define an objective threshold for the data rather than accurately estimating p-values.

277 We compared the quality of the fits across the different spatiotemporal sequences. We compared
278 the number of responsive vertices and the median goodness of fit for each individual by means of
279 repeated paired t-tests and Wilcoxon tests. We also used a correlation analyses to evaluate the
280 correspondence between the observed time series for each condition and the predicted response
281 given the stimulus location and the parameter estimates for each vertex obtained with each of the
282 mapping protocols, convolved with an HRF. To further explore the coherence of the maps obtained
283 with different mapping conditions, we computed the vertex-wise circular correlation of polar angle
284 estimates and the Pearson correlation of FWHM and beta estimates between conditions, separately
285 for each visual ROI and participant. Because vertices within a ROI are not statistically
286 independent, we calculated the inter-correlation between the time series of all ROI vertices and
287 used this information to correct the degrees of freedom of the correlation. Specifically, we
288 calculated all unique pair-wise correlations between vertices (note that we treated pairs of vertices
289 that were negatively correlated as independent, i.e. $r = 0$). We then calculated a weight for each
290 vertex by subtracting these correlations from 1 and averaging the values for all pair-wise
291 comparisons of a given vertex. Thus, in theory, if the time series of all vertices were completely
292 independent from one another, each vertex would be weighted as 1. Conversely, if all vertices were
293 identical, they would all be weighted as 0. The sum across these weights plus 1 is therefore a
294 weighted estimate of the sample size which we used to determine the degrees of freedom.
295 Moreover, we correlated the observed time courses for each condition with the predicted time
296 course given the estimated pRF parameters for each vertex in each experimental condition.
297 Finally, we compared the mean FWHM across conditions and ROIs using paired t-tests at the
298 subject level (with degrees of freedom corrected for inter-correlation between time series as
299 described above). In these analyses, we averaged FWHM across vertices encompassing different
300 eccentricities, as our mapping stimulus did not allow differentiating responses at different
301 eccentricities (i.e. each wedge had a fixed radius that covered the entire visual field mapped).

302 Results

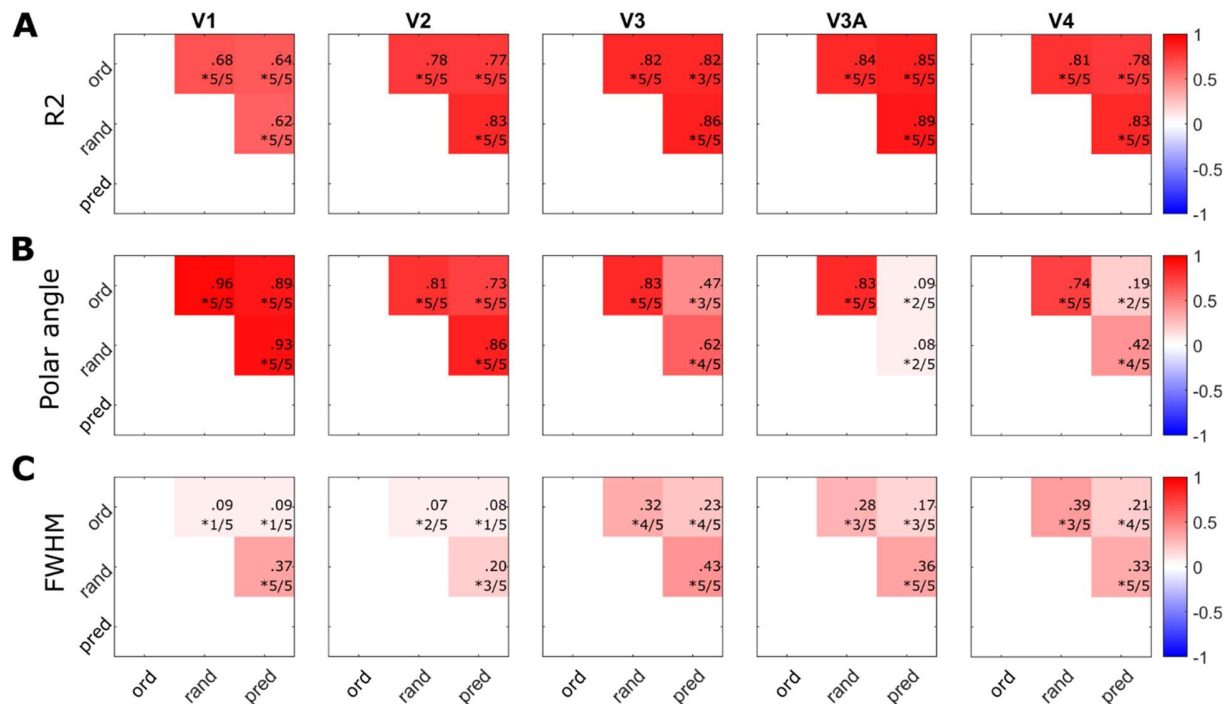
303 We obtained reliable polar angle maps with all mapping conditions for our ROIs (Figure 2).



304

305 *Figure 2. Smoothed polar angle maps for all conditions - ordered, random and predictable - in Experiment 1. In this and the*
306 *following figures, images display an inflated spherical model of the left hemisphere of participant 4 (S4).*

307 Ordered sequences provided better fits and a larger proportion of responsive vertices than the other
308 mapping sequences in all ROIs (Mean of median R^2 across ROIs: $M_{ord} = .10$, $M_{pred} = .08$, $M_{rnd} =$
309 $.08$; Mean of responsive vertices across ROIs: $M_{ord} = 35\%$, $M_{pred} = 25\%$, $M_{rnd} = 28\%$). Moreover,
310 we observed better fits for higher visual areas (Figure S 1A, D). The relatively low goodness of fit
311 obtained with this paradigm is not surprising given the high number of degrees of freedom in our
312 paradigm (due to concatenated time series rather than averaging experimental runs) and the
313 simplified model used for fitting. Importantly, all vertices considered for comparisons provided a
314 fitting that met our fixed p-value criterion of 10^{-8} in all the mapping conditions. Interestingly,
315 parameter estimates obtained with different mapping sequences performed similarly well in
316 predicting the observed time series for all mapping protocols, with generally more robust
317 predictions of the ordered sequences regardless of the mapping protocol used for the estimates
318 (Figure S 1A). Consistently, correlation analyses of model fitting results (polar angle, FWHM,
319 beta, and R^2) revealed substantial consistency across different mapping conditions in all
320 experiments and all visual areas tested. We observed high significant vertex-wise correlation
321 between R^2 ($M_{ord-rnd} = .79$, $M_{ord-pred} = .77$, $M_{rnd-pred} = .82$; Figure 3A) in different conditions for
322 all participants and ROIs ($p < .05$, Bonferroni corrected for multiple comparisons). The polar angle
323 estimates were highly robust across conditions but showed a decrease in coherence moving up in
324 the visual hierarchy for the predictable condition ($M_{ord-rnd} = .86$, $M_{ord-pred} = .56$, $M_{rnd-pred} = .68$;
325 Figure 3B).



326

327

328

329

Figure 3. Group mean correlation matrices for A) the model goodness of fit (R^2), B) polar angle estimates, and C) FWHM estimates in Experiment 1. Inset numbers (in this and the following figures) in each cell of the correlation matrix indicate the value of the average correlation and the proportion of participants that showed a significant correlation for each pair of conditions.

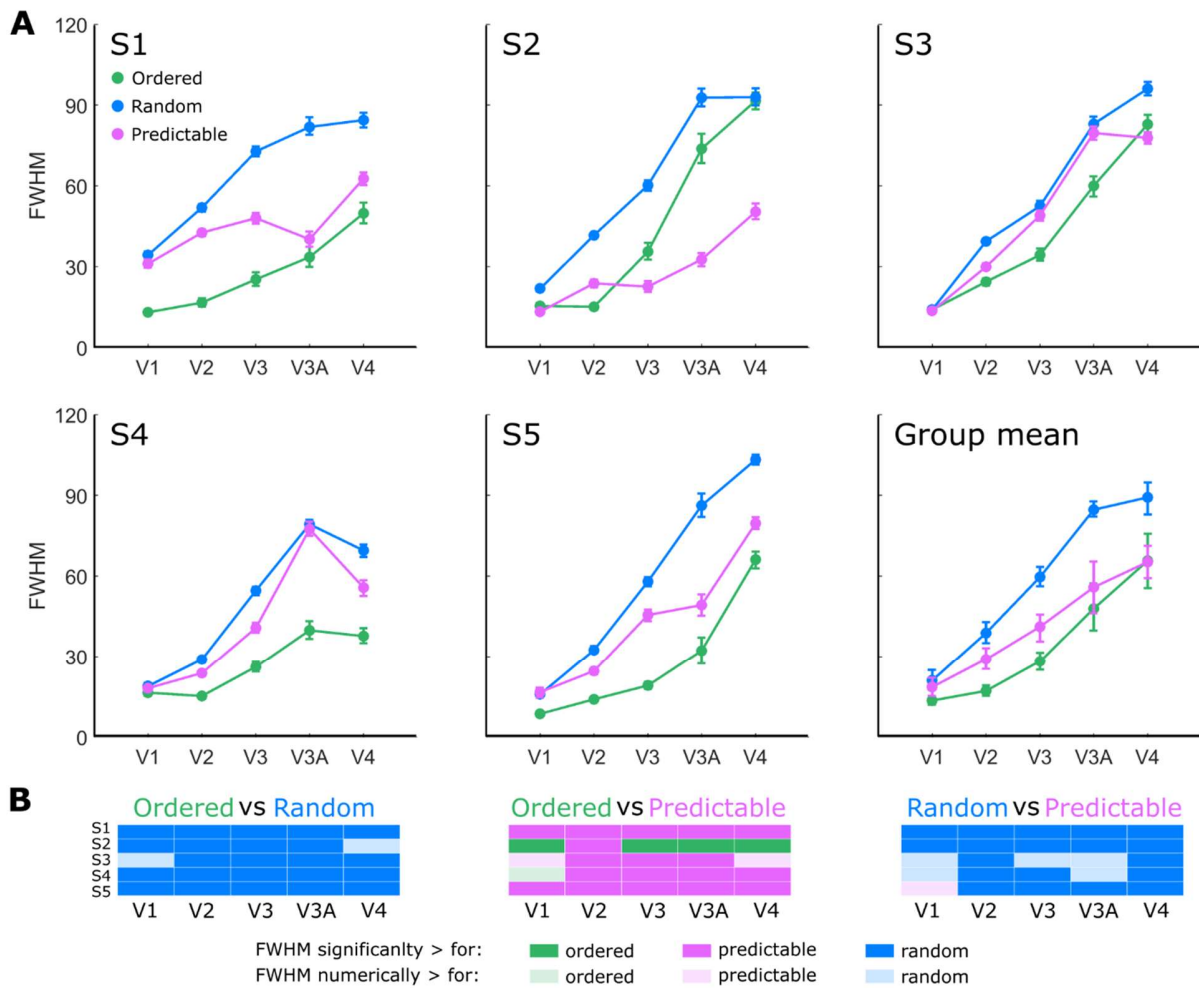
330

We observed positive but substantially weaker correlations for FWHM estimated, particularly in lower visual areas, V1-V2 ($M_{\text{ord-rand}} = .24$, $M_{\text{ord-pred}} = .17$, $M_{\text{rand-pred}} = .35$; Figure 3C).

332

We further explored potential biases and differences across mapping conditions and ROIs. As expected, FWHM estimates increased in the visual hierarchy. Interestingly, FWHM was also systematically influenced by the mapping sequence and a general pattern emerges for all visual areas (with the exception of V1 that shows noisier results) with results highly consistent across participants (Figure 4; significant results are reported for $p < .05$, Bonferroni corrected for multiple comparisons). The ordered sequence lead to significantly smaller FWHM estimates than the random sequence for most of the participants and ROIs (Figure 4B). We found similar differences between ordered and predictable sequences, although one participant showed a significant difference in the opposite direction. Interestingly, we measured smaller FWHM for predictable than random sequences (results are clearer for V2, V3 and V4).

341



342

343

344

345

346

347

Figure 4. Polar angle tuning width estimates in Experiment 1 (measured as Full-Width Half-Maximum). A) Individual and group mean FWHM estimates for different mapping sequences and visual areas. In this and the following figures, error bars in both the individual and group plots represent bootstrapped 95% confidence intervals. B) Visualisation of single subject statistics ($p < .05$ corrected for multiple comparisons).

348 Experiment 2

349 Experiment 1 revealed systematic differences in polar angle tuning functions estimated with

350 different mapping protocols. This suggests that predictability might influence the tuning response

351 of population of neurons in visual cortex. However, the predictability of our mapping sequences

352 depended on the repetition of fixed spatiotemporal structure throughout each run. Such

353 idiosyncrasies in the predictable sequences could have been responsible for relatively narrow

354 tuning width estimates (Figure 4) and the poorer agreement in polar angle estimates of this
355 sequence with the ordered and the random one (Figure 3B).

356 To address whether the fixed spatiotemporal structure of the predictable sequence was responsible
357 for the observed results, we repeated Experiment 1, but this time creating a predictable sequence
358 that was structurally indistinguishable from the random one. Rather than using a repeated
359 sequence, we rendered the sequence predictable by the use of a small visual cue. We then compared
360 the tuning width response of this sequence with the random, non-predictable one.

361 [Materials and methods](#)

362 [Participants](#)

363 Four of the original subjects took part in the two sessions of Experiment 2 (one author; age range:
364 [24-35]; 3 females). All participants had normal or corrected-to-normal visual acuity and gave
365 their written informed consent to participate to the experiment as in Experiment 1.

366 [Stimuli and Mapping sequences](#)

367 Experiment 2 was set up with the same apparatus and mapping stimuli used in Experiment 1
368 (Figure 1A). We compared four mapping sequences - ordered, predictable and two random ones.
369 Crucially, we changed how we induced the predictability of the wedge location in the predictable
370 condition. The predictable and random sequences were generated using the same algorithm, i.e.
371 wedges were presented at different locations in pseudorandom order with no adjacent locations
372 presented in a row. In contrast to Experiment 1, we generated a different sequence in each cycle
373 thus completely matching the spatiotemporal structure of random and predictable sequences. We
374 maintained the difference in predictability of the wedge locations by means of a centrally presented
375 oriented line that cued the location of the wedges (Figure 1E). The cue (0.33 x 0.07 degrees in
376 visual angle) extended from the centre of the screen. It appeared 200 ms before the onset of each
377 wedge stimulus and remained on the screen for 200 ms (Figure 1C). In the *ordered* and the
378 *predictable* conditions, the cue pointed towards the centre of the upcoming wedge. The two
379 random conditions were both unpredictable but differed for the presence or absence of the central
380 cue. In the random condition with non-predictive cue (*random-cue*), the cue pointed to the location
381 of the previous wedge. In the random condition without cue (*random-no cue*), no cue was
382 presented. Thus, neither of the random conditions contained any information about the location of
383 the upcoming wedge.

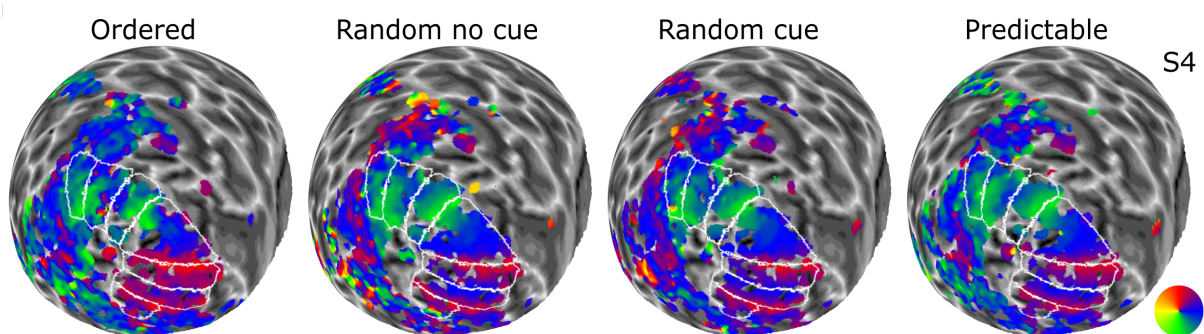
384 For all conditions, each step of the wedge was presented for 1 s such that an entire cycle was
385 completed in 8 s. Cycles were separated by fixation intervals of variable duration ranging from 1
386 to 8 s in steps of 1 s. Each functional scan consisted of 303 acquisitions. Data were collected in
387 two sessions (performed on consecutive days or one day apart) of 12 runs each taking
388 approximately 90 minutes. Each condition was repeated in 3 separate runs in each session. All
389 conditions were presented in randomized order every 4 runs.

390 Analyses

391 As in Experiment 1, we only analysed the fitted parameters of those vertices for which we obtained
392 realistic estimates ($k > 0$) and that had a goodness of fit, R^2 , higher than a critical value based on a
393 fixed p-value ($p = 10^{-8}$). This corresponds to $R^2 > 0.019$ in Experiment 2.

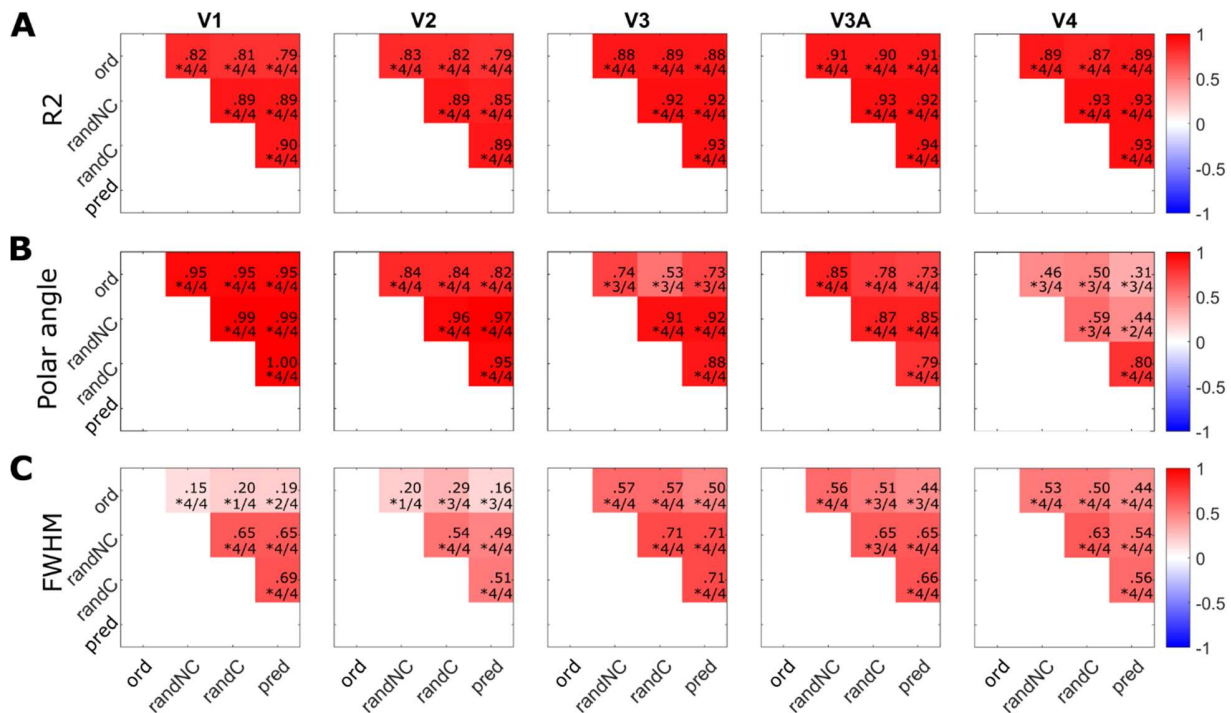
394 Results

395 Experiment 2 mostly replicated the results of Experiment 1 with even clearer polar angle maps
396 (Figure 5) and higher consistencies between parameter estimates (Figure 6), possibly due to the
397 higher number of volumes collected.



398
399 *Figure 5. Smoothed polar angle maps for all conditions - ordered, random with or without uninformative cue, and predictable - in*
400 *Experiment 2.*

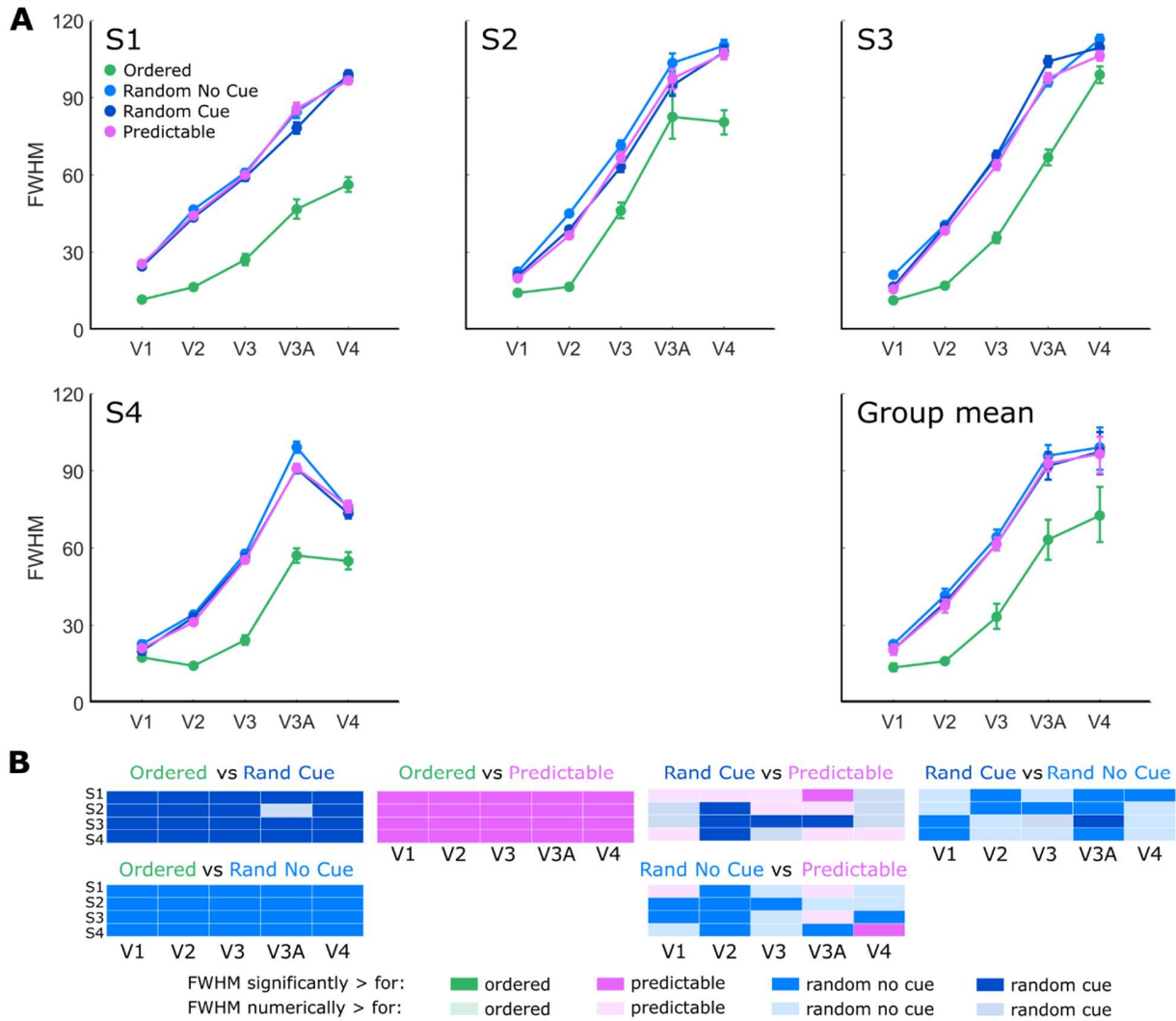
401 Ordered sequences provided better fits to the data than predictable and random sequences (Figure
402 S 1B, E; Mean of median R^2 across ROIs: $M_{ord} = .09$, $M_{pred} = .08$, $M_{randNC} = .08$, $M_{randC} = .08$; Mean
403 of responsive vertices across ROIs: $M_{ord} = 43\%$, $M_{pred} = 41\%$, $M_{randC} = 40\%$, $M_{randNC} = 37\%$).
404 However, our analyses confirmed that the parameters estimated in the different conditions
405 performed equally well in predicting the time series data (Figure S 2B).



406

407 *Figure 6. Mean correlation matrices for A) goodness of fit (R²). B) polar angle, and C) FWHM estimates in Experiment 2.*

408 We also replicated differences in FWHM estimates with different sequence structures with ordered
 409 sequences leading to systematically smaller FWHM estimates than random and predictable
 410 sequences (p < .05 corrected, for all participants and ROIs but one comparison for S2 V3A as
 411 illustrated in Figure 7 **Error! Reference source not found.**). Importantly, we did not observe any
 412 systematic differences between predictable and random sequences with the exception of V2, where
 413 FWHM were systematically smaller for predictable than random sequences as also shown in
 414 Experiment 1 (significant difference for all participants in the comparison with the random-no cue
 415 condition and with all participants but one in the random-cue condition).



416

417 *Figure 7. Polar angle tuning width estimates in Experiment 2. A) Individual and group mean FWHM estimates. B) Visualisation of*
 418 *single subject statistics ($p < .05$ corrected for multiple comparisons).*

419

420 Experiment 3

421 Experiment 2 suggested that the spatiotemporal structure of the mapping sequence, rather than its
 422 predictability is responsible for the differences in FWHM estimates. The finding that ordered
 423 sequences yielded narrower tuning widths than random sequences in both Experiment 1 and 2
 424 contrasts with previous studies. A comparison of orderly moving bars and multifocal stimuli
 425 revealed the opposite pattern of results, with the largest pRF estimates obtained with ordered
 426 sequences (Binda et al., 2013). However, it is not clear whether pRF size estimates might have

427 been affected by surround suppression of response in the multifocal stimuli (Pihlaja, Henriksson,
428 James, & Vanni, 2008). Moreover, our results might be affected by the short mapping sequences
429 we adopted. To address this hypothesis, we replicated Experiment 2 with the same mapping
430 conditions and the same participants, but we varied the size of the mapping stimulus as well as the
431 duration of the mapping cycle.

432 [Materials and methods](#)

433 [Participants](#)

434 The same four participants (including one author) that took part in Experiment 1 and 2 participated
435 also in both sessions of Experiment 3. All participants gave their written informed consent to
436 participate to the experiment.

437 [Stimuli and Mapping sequences](#)

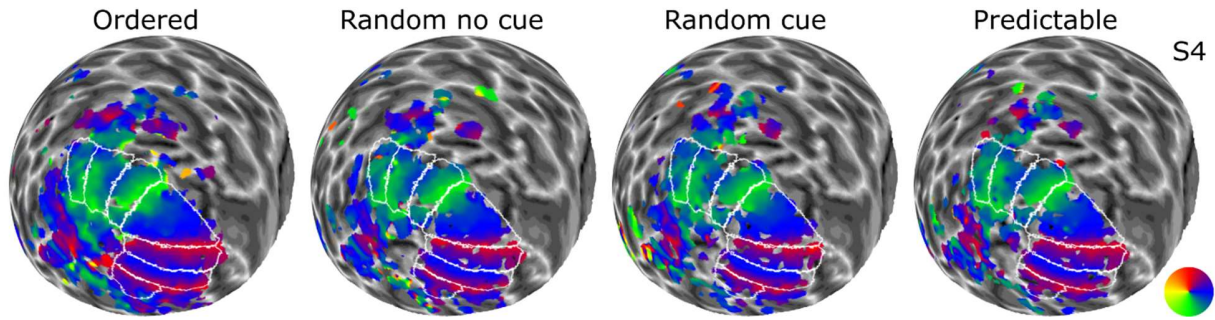
438 The mapping stimulus in Experiment 3 was a discretely moving wedge aperture subtending 6° and
439 dividing the circle in 60 non-overlapping locations, no shifts were introduced across runs (Figure
440 1B). The mapping sequences used in Experiment 3 were generated in the same way as those in
441 Experiment 2 resulting in four experimental conditions: *ordered*, *predictable*, *random-no cue*, and
442 *random-no cue* (Figure 1F). The distinctive difference between Experiment 2 and 3 is only the
443 aperture size and, consequently, the duration of the mapping cycle. For all conditions, each step of
444 the wedge was presented for 1 s such that an entire cycle was completed in 60 seconds (60 wedges
445 of 6° , 4 cycles). Cycles were separated by fixation intervals of variable duration ranging from 1 to
446 8 s in steps of 1 s. Each functional scan consisted of 295 acquisitions whilst other scanning details
447 remained identical to Experiment 2.

448 [Analyses](#)

449 As in the previous experiments, we only analysed the fitted parameters of those vertices with $k > 0$
450 and goodness of fit, $R^2 > 0.019$ (based on fixed p-value $p = 10^{-8}$).

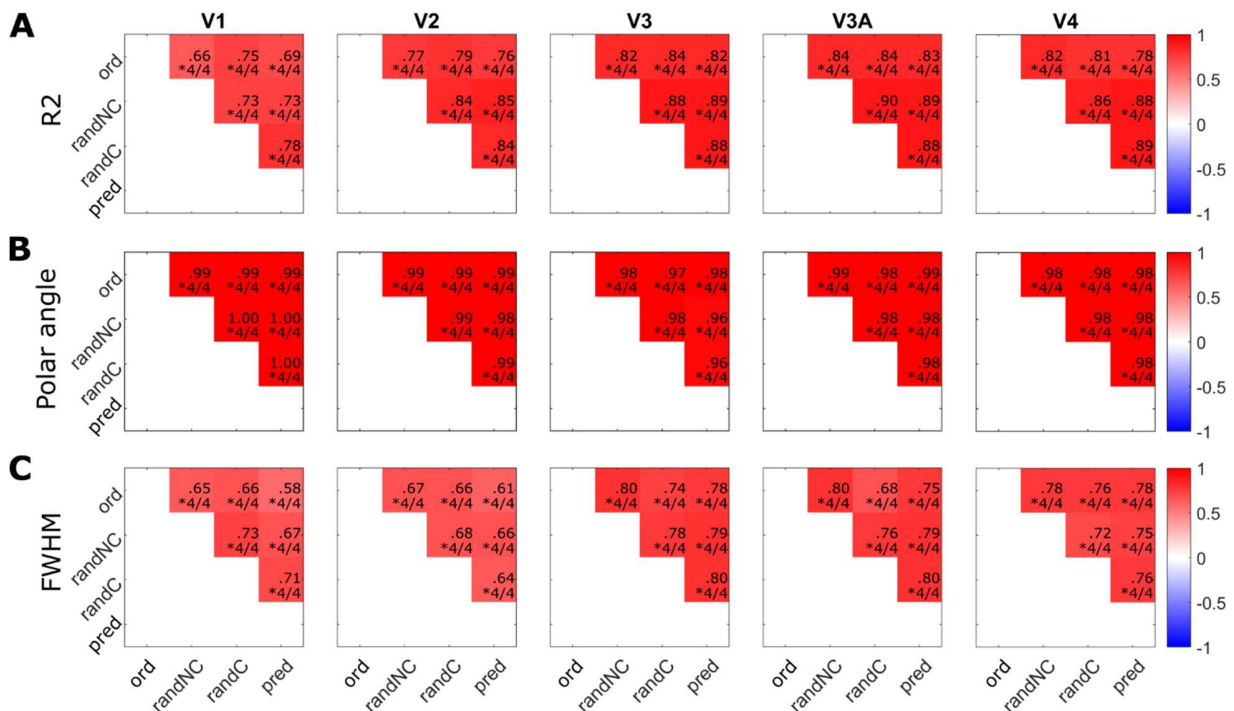
451 [Results](#)

452 Parameter estimates were consistent across mapping sequences (Figure 8, Figure 9; Figure S 2C).



453
454 Figure 8. Smoothed polar angle maps for all conditions - ordered, random with or without uninformative cue, and predictable - in
455 Experiment 3.

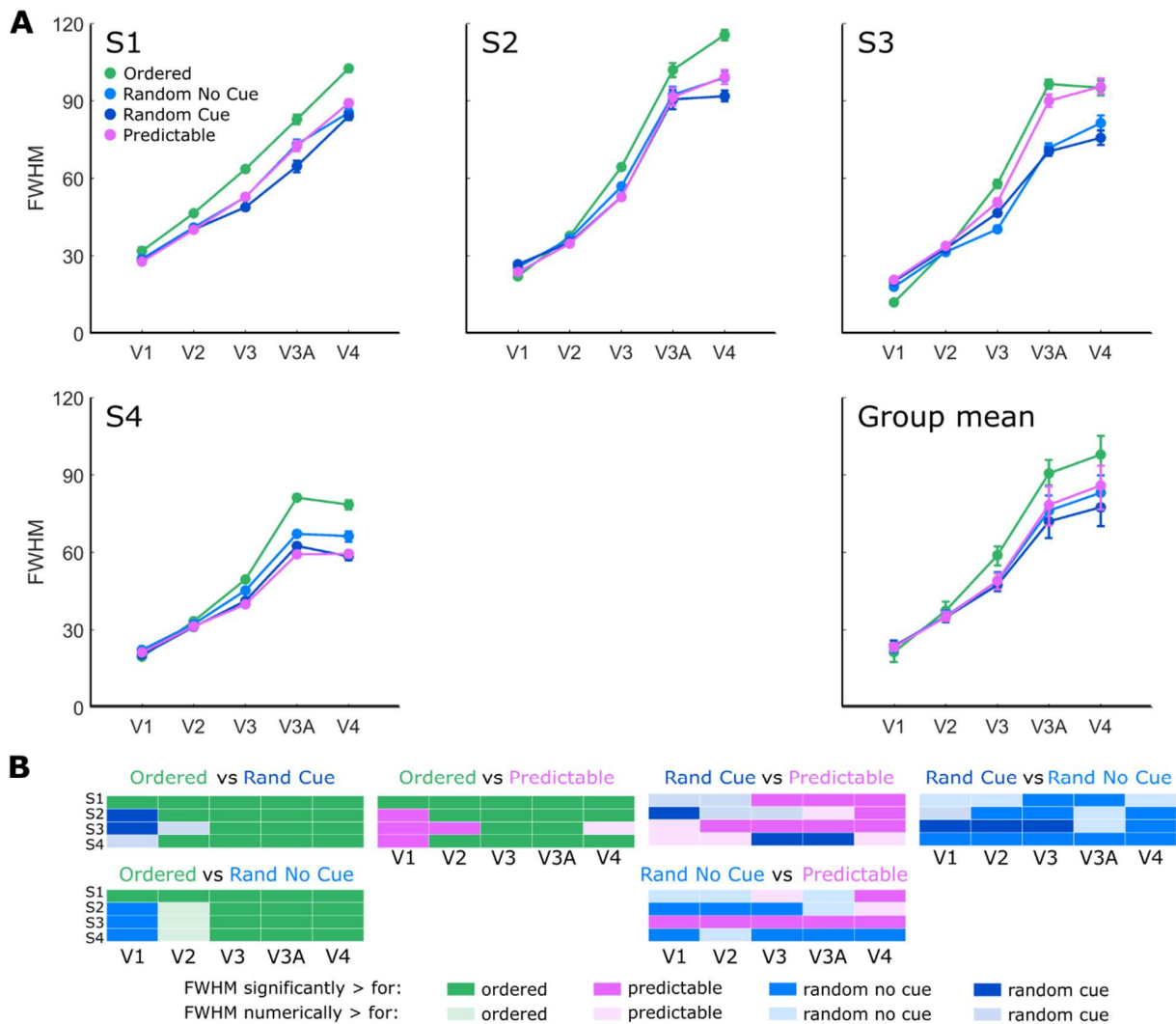
456 Ordered sequences provided much better fits to the data than predictable and random sequences
457 (Mean of median R^2 : $M_{ord} = .14$, $M_{pred} = .06$, $M_{randNC} = .06$, $M_{randC} = .06$; Mean of responsive
458 vertices across ROIs: $M_{ord} = 61\%$, $M_{pred} = 37\%$, $M_{randC} = 38\%$, $M_{randNC} = 38\%$; Figure S 1C, F).
459 However, the parameters estimated in the different conditions performed equally well in predicting
460 the time series data and they all yielded the best results when predicting the ordered sequence
461 (Figure S 2C).



462
463 Figure 9 Mean correlation matrices for A) goodness of fit (R^2). B) polar angle, and C) FWHM estimates in Experiment 3.

464 Experiment 3 produced an interesting inversion of the pattern of results in terms of FWHM
465 estimates (Figure 10) compared to the previous experiments. Although there was no consistent

466 pattern in the contrast between predictable and random sequences, FWHM estimates were
 467 systematically larger for ordered than random or predictable sequences for V3, V3A and V4.
 468 Similar results were found for V2 but with less consistent results across participants. Results for
 469 V1 were less clear but seem to suggest the opposite: FWHM were smaller for estimates obtained
 470 with an ordered rather than a random or predictable sequence.



471
 472 *Figure 10. Polar angle tuning width estimates in Experiment 3. A) Individual and group mean FWHM estimates. B) Visualisation*
 473 *of single subject statistics ($p < .05$ corrected for multiple comparisons).*

474 Simulations

475 With the following simulations, we addressed the hypothesis that the discrepancies in tuning width
 476 observed for the different mapping sequences in the previous experiments were caused by the

477 spatiotemporal properties of the haemodynamic response (Aquino, Schira, Robinson, Drysdale, &
478 Breakspear, 2012; Kriegeskorte, Cusack, & Bandettini, 2010). To test this possibility, we
479 simulated the BOLD response for Experiments 1 and 3 using the stimBOLD toolbox
480 (<https://github.com/KevinAquino/stimBOLD>, Aquino, Lacy, Robinson, & Schira, 2015). This
481 toolbox takes a visual input, predicts the cortical neural response that it evokes in early visual
482 cortex (areas V1-V3) and simulates the BOLD response taking into account the poroelastic
483 properties of the brain tissue (Aquino, Robinson, Schira, & Breakspear, 2014; Aquino et al., 2012)
484

485 Materials and methods

486 Stimuli and mapping

487 We used stimBOLD to simulate the BOLD response in visual areas V1-V3 for the left hemisphere
488 of FreeSurfer average brain (fsaverage) (Benson et al., 2012; Dale et al., 1999; Fischl et al., 1999).
489 We simulated the responses for all the conditions that differed in terms of spatiotemporal structure
490 and stimulus size in the previous experiments. In particular, we selected the ordered, random, and
491 predictable conditions in Experiment 1 – Simulation A – and the ordered and random conditions
492 of Experiment 3 – Simulation B (in both cases we employed the mapping sequences used for
493 participant 4).

494 The mapping stimulus had the same physical properties adopted in our empirical experiments (max
495 eccentricity = 8.5 dva; wedge size of 45° for Experiment 1 and 6° for Experiment 3). Each location
496 of the visual field was stimulated for 1s, before moving to the next location in the sequence. Two
497 images, selected from the original dataset of natural pictures, alternated every 500 ms.

498 Six runs for each condition were simulated separately, then Gaussian noise was added to the signal.
499 Gaussian noise was adjusted in order to produce approximately the same signal-to-noise ratio
500 (SNR) across Simulation A and B (Simulation A, $SNR_{ord} = .21$; $SNR_{pred} = .17$; $SNR_{ran} = .17$.
501 Simulation B: $SNR_{ord} = .21$; $SNR_{ran} = .11$. We computed the SNR as the ratio between the standard
502 deviation of the signal and the standard deviation of the residuals). The following analyses were
503 performed for the simulated data with and without Gaussian noise.

504

505 Analyses

506 The signal was z-score normalized and the runs concatenated before modelling the pRF profiles
507 following the same approach used for the empirical data. We focused our analyses on the

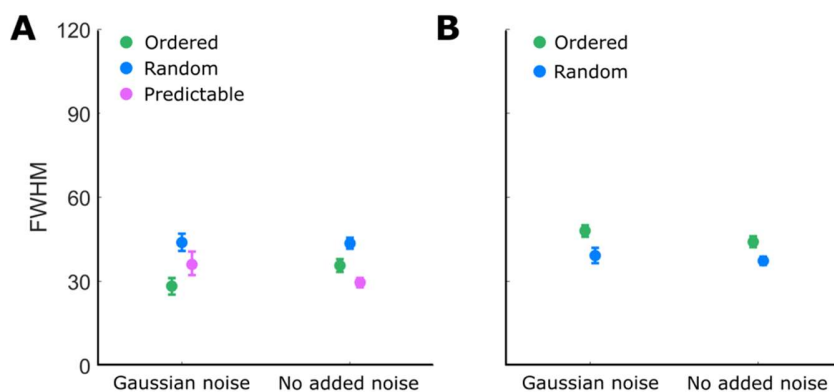
508 comparison of FWHM in the different conditions for Simulation A and B considering only those
509 vertices with goodness of fit higher than a critical value based on a fixed p-value ($p = 10^{-8}$, $R^2 >$
510 0.026 for Simulation A and $R^2 > 0.019$ for simulation B). We averaged FWHM across
511 eccentricities and ROIs (V1, V2, and V3) separately for each condition and tested their difference
512 with paired t-tests (degrees of freedom corrected for time series correlation).

513

514 Results

515 The results qualitatively replicated the difference across conditions observed in the empirical data
516 (Figure 11). In Simulation A, the ordered condition resulted in significantly lower estimates of
517 FWHM than the random condition ($V1-V3_{ord-rand}: t(196.8) = -7.05, p < .001$). The predictable
518 condition lead to intermediate results ($V1-V3_{ord-pred}: t(205.8) = -2.98, p = .003$; $V1-V3_{rand-pred}: t(200.0) = 2.97, p = .003$). Crucially, the pattern of results reversed for Simulation B with the
520 ordered condition leading to the significantly higher FWHM estimates than the random one ($V1-$
521 $V3_{ord-rand}: t(263.7) = 5.04, p < .001$). The analyses of the predicted BOLD response without
522 addition of Gaussian noise produces an inversion of the pattern of results for the ordered and
523 predictable conditions in Simulation A ($V1-V3_{ord-pred}: t(618.0) = 10.72, p < .001$; $V1-V3_{rand-pred}: t(593.0) = 10.72, p < .001$). However, the crucial difference between ordered and random
524 conditions is replicated in both simulations (Simulation A. $V1-V3_{ord-rand}: t(569.8) = -5.06, p < .001$.
525 Simulation B. $V1-V3_{ord-rand}: t(1150.7) = 5.51, p < .001$) (Figure 11).

526



527

528 *Figure 11. Polar angle tuning width estimates for simulated BOLD responses with and without added Gaussian noise. Error bars*
529 *in both the individual and group plots represent bootstrapped 95% confidence interval. A) Simulation A replicating the sequence*
530 *structure and stimulus properties of Experiment 1. B) Simulation B replicating the sequence structure and stimulus properties of*
531 *Experiment 3.*

532

533 Discussion

534 In this series of experiments, we investigated the reliability and biases of pRF modelling while
535 disambiguating the impact of predictability and spatiotemporal regularities when mapping the
536 visual cortex. We adopted a modified version of the pRF modelling approach (Dumoulin &
537 Wandell, 2008) to estimate the polar angle preference of neural populations in visual cortex and
538 designed mapping sequences characterized by different spatiotemporal structure and different
539 duration.

540 As reported in previous studies, polar angle estimates were robust across mapping sequences while
541 estimates of pRF size were more volatile (van Dijk et al., 2016). Despite their general robustness,
542 the polar angle estimates in visual areas with larger receptive fields (V3, V3A, V4) were more
543 sensitive to the structure of the mapping sequence when short mapping cycles were adopted. This
544 was particularly evident for the predictable condition in Experiment 1 in which the same short
545 sequence was repeated throughout one run introducing systematic deviations in the measured polar
546 angle estimates.

547 In all experiments, we observed striking differences in pRF size for ordered and random sequences
548 across the visual areas tested. Interestingly, in Experiment 1 we observed the narrowest tuning
549 widths for ordered mapping sequences, intermediate results for the regular and predictable
550 sequences and the widest tuning width for random sequences. These results are in contrast with
551 previous reports of larger pRF size estimates for ordered sequences (Binda et al., 2013). To test
552 whether such results were a consequence of the anticipation of the attended stimulus, we ran
553 Experiments 2 and 3 where we used a spatial cue to orient attention and matched the spatiotemporal
554 properties of predictable and random sequences. We replicated the findings for ordered and
555 random sequences only and only when a short mapping cycle was employed while the opposite
556 pattern of results emerged for slower designs. Such results argue against an impact of expectations
557 in pRF estimates and suggest that other factors may contribute to these changes in tuning width.

558 One possibility is that fast-paced designs are more susceptible to nonlinear spatiotemporal
559 interactions of responses. For example, centre-surround suppression mechanisms have been
560 suggested to modulate response amplitude when multiple stimuli are presented during mapping,
561 as happens in multi-focal designs (Pihlaja et al., 2008). Alternatively, the rapid stimulation of

562 adjacent regions might induce hemodynamic stealing (Harel, Lee, Nagaoka, Kim, & Kim, 2002),
563 or induce adaptation phenomena (Krekelberg, Boynton, & van Wezel, 2006) hence reduced BOLD
564 signal. Such phenomena could influence pRF size estimates with greater impact on ordered
565 protocols. While these possibilities are intriguing, they cannot easily explain the inversion of the
566 pattern of results observed in our last experiment. Finally, it is possible that active changes in
567 cortical vasculature might be responsible for spatiotemporal nonlinearities in the BOLD response
568 and significantly affect the pRF estimates, particularly with small voxel sizes (Aquino et al., 2012;
569 Kriegeskorte et al., 2010). Our simulations found general support for the last hypothesis indicating
570 a possible mechanism by which the interplay of stimulus properties and mapping sequence can
571 have a measurable impact of pRF estimates.

572 In our study we did not find any clear evidence that the predictability of stimulus location can
573 significantly bias polar angle or tuning width estimates. This result contradicts previous studies
574 that showed attention can cause both a shift of the preferred location towards the attended location
575 and an increase in pRF size (Kay et al., 2015; Klein et al., 2014; Sheremata & Silver, 2015; van
576 Es et al., 2018; Vo et al., 2017). Such modulation had initially reported only been in the ventral
577 cortex, higher up in the visual cortex (Kay et al., 2015) while more recent evidence suggest that
578 both feature-based and spatial-based spatial attention can induce significant shifts in the response
579 of neurons in areas as early as V1-V3 (van Es et al., 2018). It has been suggested that these changes
580 are functional to increase the precision of the representation of the target at the attended location
581 (Kay et al., 2015). While our design was not tailored to detect systematic changes in polar angle
582 preferences, we hypothesized that the predictability of the mapping sequence would affect the
583 tuning of neuronal responses. The discrepancy between our results and recent observations of
584 attentional effects can be explained by a difference in task requirements among the studies. All
585 former studies manipulated the focus of attention by varying the location at which participants
586 were performing a perceptual task, either at fixation or on the mapping stimulus (Kay et al., 2015;
587 Sheremata & Silver, 2015; van Es et al., 2018). Such demanding tasks required a redistribution of
588 resources at the attended location. On the contrary, in our experiments, our task did not require a
589 fine discrimination and the predictability of stimulus location was not strategically relevant for
590 performing the task. Thus, expectations alone may not dynamically change pRF properties in early
591 visual cortex to a significant extent, as long as there is no computational requirement for that.

592 Irrespective of the specific sequence, the fitting results described in the current study produced
593 weaker fits than standard mapping approaches (Dumoulin & Wandell, 2008). Several reasons
594 could contribute to these results. First, R^2 depends considerably on the degrees of freedom. In our
595 experiments, we concatenated the BOLD response in separate runs of the same condition leading
596 to a large number of time points per condition (up to 1818 in Experiment 2) massively increasing
597 the degrees of freedom and generally reducing R^2 for at statistical significance levels equivalent to
598 other studies. Second, in order to facilitate learning of the predictable sequences, we designed
599 protocols with unusually short cycles in Experiment 1 while long cycles but thin mapping stimuli
600 were employed in the last study. Despite these limitations, we obtained reliable maps in all
601 conditions (Figure 2, Figure 5, Figure 8).

602 Our study shows that pRF estimates are susceptible to the spatiotemporal properties of the mapping
603 sequence. In particular, ordered and random mapping protocols show different susceptibility to
604 other design choices such as stimulus type and duration of the mapping cycle and can produce
605 significantly different pRF results. Finally, it is worth noting that while ordered sequences are
606 typically preferred for their higher goodness of fit, this is not a guarantee of their robustness. More
607 specifically, the pRF estimates obtained with different sequences, both ordered and random,
608 performed comparably well in predicting the response to different mapping stimuli. To conclude,
609 depending on other design constraints, one should consider which protocol is more suitable for the
610 experimental purposes.

611

612 [Acknowledgments](#)

613 Supported by ERC Starting Grant (310829) to DSS. We thank Kevin Aquino for his support with
614 the use of the BOLD simulation toolbox (stimBOLD).

615

616 Bibliography

617

618 Alvarez, I., de Haas, B., Clark, C. A., Rees, G., & Schwarzkopf, D. S. (2015). Comparing different
619 stimulus configurations for population receptive field mapping in human fMRI. *Frontiers in*
620 *Human Neuroscience*, 9(February), 96. <https://doi.org/10.3389/fnhum.2015.00096>

621 Amano, K., Wandell, B. a, & Dumoulin, S. O. (2009). Visual field maps, population receptive field
622 sizes, and visual field coverage in the human MT+ complex. *Journal of Neurophysiology*,
623 102(5), 2704–2718. <https://doi.org/10.1152/jn.00102.2009>

624 Anderson, E. J., Tibber, M. S., Schwarzkopf, D. S., Shergill, S. S., Fernandez-Egea, E., Rees, G., &
625 Dakin, S. C. (2016). Visual population receptive fields in people with schizophrenia have
626 reduced inhibitory surrounds. *The Journal of Neuroscience*, 37(6), 3620–15.
627 <https://doi.org/10.1523/JNEUROSCI.3620-15.2016>

628 Aquino, K. M., Lacy, T. C., Robinson, P. A., & Schira, M. M. (2015). Using models to design fMRI
629 experiments - not just fit data. In *21st Annual Meeting of the Organization for Human*
630 *Brain Mapping*.

631 Aquino, K. M., Robinson, P. A., Schira, M. M., & Breakspear, M. (2014). Deconvolution of neural
632 dynamics from fMRI data using a spatiotemporal hemodynamic response function.
633 *NeuroImage*, 94, 203–215. <https://doi.org/10.1016/j.neuroimage.2014.03.001>

634 Aquino, K. M., Schira, M. M., Robinson, P. A., Drysdale, P. M., & Breakspear, M. (2012).
635 Hemodynamic traveling waves in human visual cortex. *PLoS Computational Biology*, 8(3).
636 <https://doi.org/10.1371/journal.pcbi.1002435>

637 Benson, N. C., Butt, O. H., Datta, R., Radoeva, P. D., Brainard, D. H., & Aguirre, G. K. (2012). The
638 retinotopic organization of striate cortex is well predicted by surface topology. *Current*
639 *Biology*, 22(21), 2081–2085. <https://doi.org/10.1016/j.cub.2012.09.014>

640 Binda, P., Thomas, J. M., Boynton, G. M., & Fine, I. (2013). Minimizing biases in estimating the
641 reorganization of human visual areas with BOLD retinotopic mapping. *Journal of Vision*,
642 13(7), 1–16. <https://doi.org/10.1167/13.7.13>

643 Brainard, D. H. (1997). The Psychophysics Toolbox. *Spatial Vision*, 10, 433–436.
644 <https://doi.org/10.1163/156856897X00357>

- 645 Breuer, F. A., Blaimer, M., Heidemann, R. M., Mueller, M. F., Griswold, M. A., & Jakob, P. M.
646 (2005). Controlled aliasing in parallel imaging results in higher acceleration (CAIPIRINHA)
647 for multi-slice imaging. *Magnetic Resonance in Medicine*, 53(3), 684–691.
648 <https://doi.org/10.1002/mrm.20401>
- 649 Dale, A. M., Fischl, B., & Sereno, M. I. (1999). Cortical surface-based analysis: I. Segmentation
650 and surface reconstruction. *NeuroImage*, 9(2), 179–194.
651 <https://doi.org/10.1006/nimg.1998.0395>
- 652 de Haas, B., Schwarzkopf, D. S., Anderson, E. J., & Rees, G. (2014). Perceptual load affects
653 spatial tuning of neuronal populations in human early visual cortex. *Current Biology*, 24(2),
654 R66–R67. <https://doi.org/10.1016/j.cub.2013.11.061>
- 655 Dekker, T. M., Schwarzkopf, D. S., de Haas, B., Nardini, M., & Sereno, M. I. (2017). Population
656 receptive field tuning properties of visual cortex during childhood. *BioRxiv:2132108*.
657 <https://doi.org/10.1101/213108>
- 658 Dekker, T. M., Schwarzkopf, D. S., de Haas, B., Nardini, M., & Sereno, M. I. (2019). Population
659 receptive field tuning properties of visual cortex during childhood. *Developmental*
660 *Cognitive Neuroscience*, (July 2018), 100614. <https://doi.org/10.1016/j.dcn.2019.01.001>
- 661 Dumoulin, S. O., & Knapen, T. (2018). How Visual Cortical Organization Is Altered by
662 Ophthalmologic and Neurologic Disorders. *Annual Review of Vision Science*, 4(1), annurev-
663 vision-091517-033948. <https://doi.org/10.1146/annurev-vision-091517-033948>
- 664 Dumoulin, S. O., & Wandell, B. A. (2008). Population receptive field estimates in human visual
665 cortex. *NeuroImage*, 39(2), 647–660. <https://doi.org/10.1016/j.neuroimage.2007.09.034>
- 666 Ekman, M., Kok, P., & de Lange, F. P. (2017). Time-compressed preplay of anticipated events in
667 human primary visual cortex. *Nature Communications*, 8(May), 15276.
668 <https://doi.org/10.1038/ncomms15276>
- 669 Engel, S. A., Rumelhart, D. E., Wandell, B. A., Lee, A. T., Glover, G. H., Chichilnisky, E.-J., &
670 Shadlen, M. N. (1994). fMRI of human visual cortex. *Nature*.
671 <https://doi.org/10.1038/369525a0>
- 672 Fischl, B., Sereno, M. I., & Dale, A. M. (1999). Cortical surface-based analysis: II. Inflation,
673 flattening, and a surface-based coordinate system. *NeuroImage*, 9(2), 195–207.

- 674 <https://doi.org/10.1006/nimg.1998.0396>
- 675 Gomez, J., Natu, V., Jeska, B., Barnett, M., & Grill-Spector, K. (2018). Development differentially
676 sculpts receptive fields across early and high-level human visual cortex. *Nature*
677 *Communications*, 9(1), 788. <https://doi.org/10.1038/s41467-018-03166-3>
- 678 Harel, N., Lee, S. P., Nagaoka, T., Kim, D. S., & Kim, S. G. (2002). Origin of negative blood
679 oxygenation level-dependent fMRI signals. *Journal of Cerebral Blood Flow and Metabolism*,
680 22(8), 908–917. <https://doi.org/10.1097/00004647-200208000-00002>
- 681 Harvey, B. M., & Dumoulin, S. O. (2011). The relationship between cortical magnification factor
682 and population receptive field size in human visual cortex: constancies in cortical
683 architecture. *J Neurosci*, 31(38), 13604–13612. [https://doi.org/10.1523/JNEUROSCI.2572-](https://doi.org/10.1523/JNEUROSCI.2572-11.2011)
684 11.2011
- 685 Kastner, S., Pinsk, M. A., De Weerd, P., Desimone, R., & Ungerleider, L. G. (1999). Increased
686 activity in human visual cortex during directed attention in the absence of visual
687 stimulation. *Neuron*, 22(4), 751–61. [https://doi.org/http://dx.doi.org/10.1016/S0896-](https://doi.org/http://dx.doi.org/10.1016/S0896-6273(00)80734-5)
688 6273(00)80734-5
- 689 Kay, K. N., Weiner, K. S., & Grill-Spector, K. (2015). Attention reduces spatial uncertainty in
690 human ventral temporal cortex. *Current Biology*, 25(5), 595–600.
691 <https://doi.org/10.1016/j.cub.2014.12.050>
- 692 Klein, B. P., Harvey, B. M., & Dumoulin, S. O. (2014). Attraction of position preference by spatial
693 attention throughout human visual cortex. *Neuron*, 84(1), 227–237.
694 <https://doi.org/10.1016/j.neuron.2014.08.047>
- 695 Krekelberg, B., Boynton, G. M., & van Wezel, R. J. A. (2006). Adaptation: from single cells to
696 BOLD signals. *Trends in Neurosciences*, 29(5), 250–256.
697 <https://doi.org/10.1016/j.tins.2006.02.008>
- 698 Kriegeskorte, N., Cusack, R., & Bandettini, P. (2010). NeuroImage How does an fMRI voxel
699 sample the neuronal activity pattern : Compact-kernel or complex spatiotemporal filter ?
700 *NeuroImage*, 49(3), 1965–1976. <https://doi.org/10.1016/j.neuroimage.2009.09.059>
- 701 Moutsiana, C., de Haas, B., Papageorgiou, A., van Dijk, J. A., Balraj, A., Greenwood, J. A., &
702 Schwarzkopf, D. S. (2016). Cortical idiosyncrasies predict the perception of object size.

- 703 *Nature Communications*, 7, 1–25. <https://doi.org/10.1101/026989>
- 704 Pelli, D. G. (1997). The VideoToolbox software for visual psychophysics: transforming numbers
705 into movies. *Spatial Vision*, 10, 437–442. <https://doi.org/10.1163/156856897X00366>
- 706 Pihlaja, M., Henriksson, L., James, A. C., & Vanni, S. (2008). Quantitative multifocal fMRI shows
707 active suppression in human V1. *Human Brain Mapping*, 29(9), 1001–1014.
708 <https://doi.org/10.1002/hbm.20442>
- 709 Schwarzkopf, D. S., Anderson, E. J., de Haas, B., White, S. J., & Rees, G. (2014). Larger
710 Extrastriate Population Receptive Fields in Autism Spectrum Disorders. *Journal of*
711 *Neuroscience*, 34(7), 2713–2724. <https://doi.org/10.1523/JNEUROSCI.4416-13.2014>
- 712 Sereno, M. I., Dale, a M., Reppas, J. B., Kwong, K. K., Belliveau, J. W., Brady, T. J., ... Tootell, R. B.
713 H. (1995). Borders of Multiple Visual Areas in Humans Revealed by Functional Magnetic
714 Resonance Imaging Borders of Multiple Visual Areas in Humans Revealed by Functional
715 Magnetic Resonance Imaging. *Science*, 268(5212), 889–893.
- 716 Sereno, M. I., McDonald, C. T., & Allman, J. M. (1994). Analysis of Retinotopic Maps in
717 Extrastriate Cortex. *Cerebral Cortex*, 4(6), 601–620.
718 <https://doi.org/10.1093/cercor/4.6.601>
- 719 Sheremata, S. L., & Silver, M. A. (2015). Hemisphere-Dependent Attentional Modulation of
720 Human Parietal Visual Field Representations. *Journal of Neuroscience*, 35(2), 508–517.
721 <https://doi.org/10.1523/JNEUROSCI.2378-14.2015>
- 722 Silson, E. H., Reynolds, R. C., Kravitz, D. J., & Baker, C. I. (2018). Differential sampling of visual
723 space in ventral and dorsal early visual cortex. *The Journal of Neuroscience*, 38(9), 2717–
724 17. <https://doi.org/10.1523/JNEUROSCI.2717-17.2018>
- 725 Silva, M. F., Brascamp, J. W., Ferreira, S., Castelo-Branco, M., Dumoulin, S. O., & Harvey, B. M.
726 (2018). Radial asymmetries in population receptive field size and cortical magnification
727 factor in early visual cortex. *NeuroImage*, 167(September 2016), 41–52.
728 <https://doi.org/10.1016/j.neuroimage.2017.11.021>
- 729 Smittenaar, C. R., Macsweeney, M., Sereno, M. I., & Schwarzkopf, D. S. (2016). Does Congenital
730 Deafness Affect the Structural and Functional Architecture of Primary Visual Cortex? *The*
731 *Open Neuroimaging Journal*, 10(16), 1–19.

- 732 <https://doi.org/10.2174/1874440001610010001>
- 733 Thomas, J. M., Huber, E., Stecker, G. C., Boynton, G. M., Saenz, M., & Fine, I. (2015). Population
734 receptive field estimates of human auditory cortex. *NeuroImage*, *105*, 428–439.
735 <https://doi.org/10.1016/j.neuroimage.2014.10.060>
- 736 van Dijk, J. A., de Haas, B., Moutsiana, C., & Schwarzkopf, D. S. (2016). Intersession reliability of
737 population receptive field estimates. *NeuroImage*, *143*, 293–303.
738 <https://doi.org/10.1016/j.neuroimage.2016.09.013>
- 739 van Es, Theeuwes, J., & Knapen, T. (2018). Spatial sampling in human visual cortex is modulated
740 by both spatial and feature-based attention.
- 741 Vanni, S., Henriksson, L., & James, A. C. (2005). Multifocal fMRI mapping of visual cortical areas.
742 *NeuroImage*, *27*(1), 95–105. <https://doi.org/10.1016/j.neuroimage.2005.01.046>
- 743 Vo, V. A., Sprague, T. C., & Serences, J. T. (2017). Spatial Tuning Shifts Increase the
744 Discriminability and Fidelity of Population Codes in Visual Cortex. *The Journal of*
745 *Neuroscience*, *37*(12), 3386–3401. <https://doi.org/10.1523/JNEUROSCI.3484-16.2017>
- 746 Wandell, B. A., & Winawer, J. (2015). Computational neuroimaging and population receptive
747 fields. *Trends in Cognitive Sciences*, *19*(6), 349–357.
748 <https://doi.org/10.1016/j.tics.2015.03.009>
- 749 Yildirim, F., Carvalho, J., & Cornelissen, F. W. (2018). A second-order orientation-contrast
750 stimulus for population-receptive-field-based retinotopic mapping. *NeuroImage*,
751 *164*(May), 183–193. <https://doi.org/10.1016/j.neuroimage.2017.06.073>
- 752 Zeidman, P., Silson, E. H., Schwarzkopf, D. S., Baker, C. I., & Penny, W. (2018). Bayesian
753 population receptive field modelling. *NeuroImage*, *180*(September), 173–187.
754 <https://doi.org/10.1016/j.neuroimage.2017.09.008>
- 755 Zuiderbaan, W., Harvey, B. M., & Dumoulin, S. O. (2012). Modeling center – surround con fi
756 gurations in population receptive fi elds using fMRI. *Journal of Vision*, *12*(3), 1–15.
757 <https://doi.org/10.1167/12.3.10.Introduction>
- 758

759 Supplementary Materials

760

761 Control analyses and results

762 In all three experiments, to ensure consistency in fixation stability and task engagement across
763 conditions, we measured target detection accuracy in the dual-task across conditions. Moreover,
764 we measured the mean absolute deviation of eye position from fixation along the x and y axes in
765 degrees of visual angle (dva).

766 In Experiment 1, we did not observe noticeable differences in participants' accuracy in performing
767 the dual-task (p(Hit): $M_{ord}(SD) = .77 (.11)$, $M_{pred}(SD) = .74(.14)$, $M_{rand}(SD) = .81(.05)$) nor in
768 stability of fixation (Absolute deviation from fixation along in dva. Deviation along x axis:
769 $M_{ord}(SD) = .28(.15)$; $M_{pred}(SD) = .24(.11)$; $M_{rand}(SD) = .25(.10)$. Deviation along y axis: $M_{ord}(SD)$
770 $= .46(.42)$, $M_{pred}(SD) = .41(.33)$, $M_{rand}(SD) = .36(.26)$) across conditions.

771 Similarly, in Experiment 2, we did not observe significant differences in participants' accuracy in
772 the dual-task (p(Hit): $M_{ord}(SD) = .72 (.16)$, $M_{pred}(SD) = .74(.17)$, $M_{randNC}(SD) = .68(.08)$,
773 $M_{randC}(SD) = .69(.14)$) nor in stability of fixation (Absolute deviation from fixation along in dva.
774 Deviation along x axis: $M_{ord}(SD) = .21(.08)$, $M_{pred}(SD) = .19(.06)$, $M_{randNC}(SD) = .23(.09)$,
775 $M_{randC}(SD) = .21(.09)$. Deviation along y axis: $M_{ord}(SD) = .31(.23)$, $M_{pred}(SD) = .30(.20)$,
776 $M_{randNC}(SD) = .32(.20)$, $M_{randC}(SD) = .34(.24)$) across conditions.

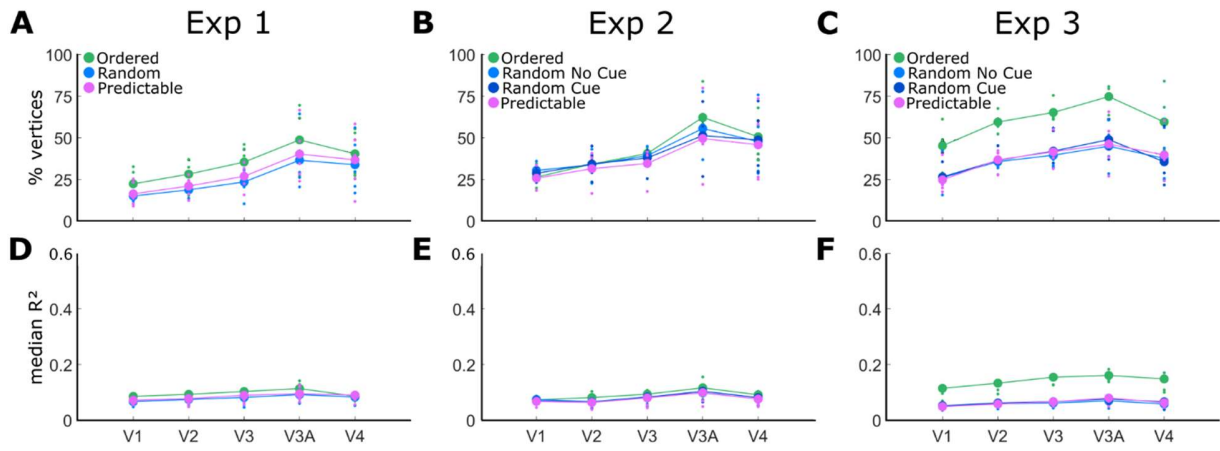
777 Consistent with the previous experiments, also in Experiment 3, we did not observe significant
778 differences in participants' accuracy in the dual-task (p(Hit): $M_{ord}(SD) = .89 (.07)$, $M_{pred}(SD)$
779 $= .86(.15)$, $M_{randNC}(SD) = .89(.12)$, $M_{randC}(SD) = .93(.06)$) nor in stability of fixation (Absolute
780 deviation from fixation along in dva. Deviation along x axis: $M_{ord}(SD) = .23(.12)$, $M_{pred}(SD)$
781 $= .24(.10)$, $M_{randNC}(SD) = .32(.21)$, $M_{randC}(SD) = .27(.13)$. Deviation along y axis: $M_{ord}(SD) =$
782 $.31(.22)$, $M_{pred}(SD) = .42(.38)$, $M_{randNC}(SD) = .54(.61)$, $M_{randC}(SD) = .37(.58)$) across conditions.

783

784

785

786



787

788 *Figure S 1 Data quality in Experiments 1-3. (A-C) Percentage of responsive vertices in each visual area and condition tested. (D-F)*

789 *Median goodness of fit (R^2). Large dots indicate mean group results and small dots indicate individual participants' data. Ordered*

790 *(green), random (blue) and predictable (fuchsia) sequences are displayed for all experiments. In Experiments 2 and 3, the light*

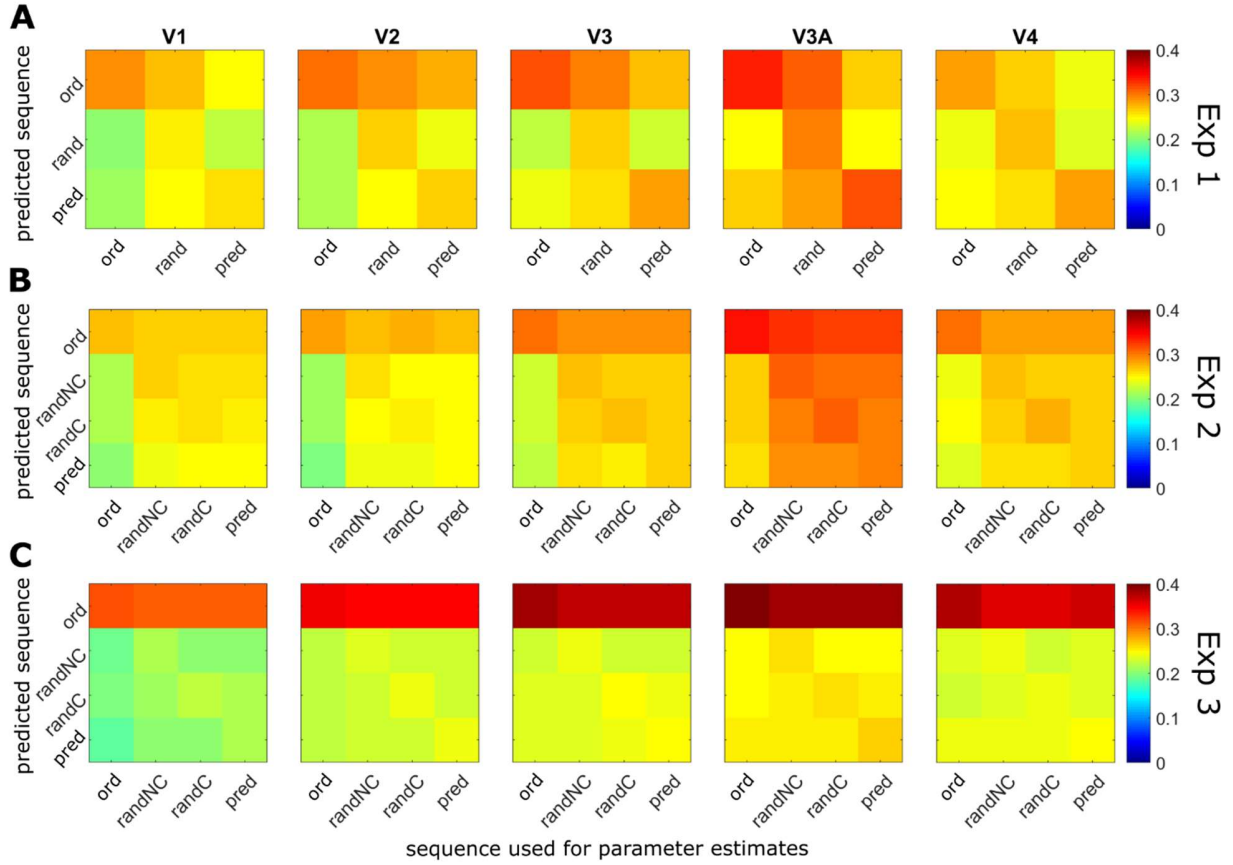
791 *blue dots and the dark blue dots depict results for the random no-cue and random cue conditions respectively.*

792

793

794

795



796

797

798

799

800

801

802

Figure S 2 Group mean Pearson correlation matrices of predicted and observed time series in Experiments 1-3. The parameters obtained from fitting each of the mapping sequences (x-axis) are employed to generate time series for each of the conditions in the experiment. The resulting predicted responses are then correlated with the measured time series (y-axis). In all experiments, the ordered sequences are predicted with more accuracy than any of the other sequences irrespective of the parameters used for generating the times series.